BIOCHEMISTRY

Structural analysis of HER2-trastuzumab complex reveals receptor conformational adaptation

Santiago Vacca[1]†, Marcos Gragera[2]†, Alejandro Buschiazzo[3,4], David Herreros[2], James M. Krieger[2], Santiago Bonn-Garcia[1], Roberto Melero[2], Carlos OS. Sorzano[2], Jose M. Carazo[2]*, Ohad Medalia[1]*, Andreas Plückthun[1]*

Human epidermal growth factor receptor-2 (HER2) is a receptor tyrosine kinase, associated with a variety of malignant tumors, usually through overexpression, resulting in aberrant signaling. Trastuzumab (TZB), one of the monoclonal antibodies (mAbs) used in combination with chemotherapy, has become a major therapeutic for HER2-overexpressing cancers. Current structural understanding of HER2 and its interactions with other receptors and with different affinity agents has relied on numerous structures of individual domains of HER2. Here, we subjected purified near full-length HER2 to single-particle cryo–electron microscopy (cryo-EM) analysis. Besides the canonical conformation described in previous structural studies, we report a previously unreported conformation of the HER2 extracellular domain that is stabilized upon TZB binding, which might hamper association with HER3, a receptor with which HER2 forms an oncogenic unit. Together, our findings provide insights into the conformational dynamics of the HER2 receptor and the mechanism of action of TZB.

INTRODUCTION

Epidermal growth factor receptors (EGFRs) have been thoroughly studied for their involvement in the development of various human tumors. They belong to subclass I of the superfamily of receptor tyrosine kinases, consisting of four members. These include the human epidermal growth factor receptor-1 (HER1 or EGFR/ErbB1), HER2 (ErbB2/neu), HER3 (ErbB3), and HER4 (ErbB4), all of which are involved in a complex regulation network that modulates cell growth, differentiation, migration, and survival (*1*, *2*). Ligand binding is typically required for dimerization and subsequent downstream signaling of these receptors, except for HER2.

HER2 is an exception among the EGFR family, as it is the only member with no natural known ligand. Extensive crystallographic and molecular dynamics data have shown that HER2 folds into a constitutively active extended conformation, in contrast to the other EGFR family members (*2*–*4*). Direct interactions between subdomains I and III, which are necessary to maintain this extended conformation in HER2, were revealed in the crystal structure (*5*). An absence of interactions between subdomains II and IV, which are required for the receptor to adopt a tethered conformation (*5*), was also observed. By being always poised for dimerization, and not itself being regulated by ligands, HER2 becomes the preferred heterodimerization partner for all EGFR family members (*6*).

Set apart from other EGFR family members, HER2 has garnered substantial pharmacological interest. Overexpression of HER2 has been implicated in the development and progression of tumor cells and is commonly associated with aggressive forms of breast and gastric cancers (*7*, *8*). HER2 has therefore been recognized as a prime candidate for tumor-targeting therapeutics, since ~20 to 30% of breast cancers and ~20% of gastric cancers exhibit HER2 overexpression, usually correlated with rapid disease progression and poor survival (*9*–*12*). Over the past few decades, small-molecule tyrosine kinase inhibitors (*13*–*15*) and humanized monoclonal antibodies (mAbs) (*9*, *16*) have been developed to target HER2-overexpressing cells. While kinase inhibitors have resulted in low clinical efficacies during clinical trials (*17*–*19*), anti-HER2 mAbs have become an integral part of the standard of care for HER2-positive breast cancers. Combined therapies of mAbs with chemotherapy have turned out to be more efficacious in treating HER2-positive breast cancer (*20*–*22*), and HER2-directed antibody-drug conjugates (ADC) have been added to the armamentarium of treatments (*23*).

The mAbs bind to the HER2 extracellular domain (ECD), inhibiting dimerization with HER3, a binding partner for HER2-driven tumorigenesis, under certain circumstances. In particular, pertuzumab (PZB) blocks the HER2-HER3 dimerization interface, while trastuzumab (TZB) binds to subdomain IV and disrupts the heterodimer in the absence of a ligand for HER3 (*20*, *24*–*30*). The HER2-HER3 dimer functions as an oncogenic unit, where overexpressed HER2 (which, as mentioned, has no natural ligand) phosphorylates HER3, whose kinase is nearly devoid of activity (*26*). Current structural knowledge about HER2 and its interactions with specific therapeutic agents is derived from numerous studies with individual HER2 domains, notably the ECD, transmembrane region, and kinase domain (*5*, *31*–*36*). A single study (*30*) has investigated the heterodimerization of HER2 with HER3 in the presence and absence of the major therapeutic mAbs, using near full-length constructs, but only the ECDs were resolved. The dimerization arm, located in subdomain II, is a major interface for dimerization in the EGFR family. Except for HER2, the dimerization arm of other EGFR family members is only made accessible in a stable form when a receptor is bound to a cognate ligand, although some structural fluctuations have been hypothesized in the absence of ligand (*37*). Therefore, stable receptor heterodimerization is normally only possible in the presence of a ligand, such as neuregulin-1β (NRG1β) (*30*).

However, upon overexpression of HER2, and in the absence of ligands, it has been shown that one of the main therapeutic mAbs,

[1]Department of Biochemistry, University of Zürich, Winterthurerstrasse 190, CH-8057 Zürich, Switzerland. [2]Centro Nacional de Biotecnología (CNB), CSIC, 28049, Madrid, Spain. [3]Institut Pasteur de Montevideo, Laboratory of Molecular and Structural Microbiology, 11400 Montevideo, Uruguay. [4]Department of Microbiology, Institut Pasteur, 75015 Paris, France.
*Corresponding author. Email: carazo@cnb.csic.es (J.M.C.); omedalia@bioc.uzh.ch (O.M.); plueckthun@bioc.uzh.ch (A.P.)
†These authors contributed equally to this work.

TZB, can inhibit phosphorylation of HER3 and, by implication, the formation of the oncogenic unit (*38*). It has therefore been suggested that TZB may disrupt the formation of an unliganded HER2-HER3 dimer (*38*), although the structural details were unknown. In the presence of a ligand, however, TZB loses this ability to prevent HER3 phosphorylation, consistent with the finding of a liganded HER2-HER3-TZB structure (*30*). The gap of knowledge in the structural influence of this mAb on HER2 motivated us to investigate the structure of near full-length complexes of HER2 in the absence and presence of TZB.

Several structures of the HER2 ECD in complex with the Fab fragment of TZB, which binds to the ECD subdomain IV, have been previously published, all of which report a similar conformation of the HER2 ECD (*5*, *30*, *31*, *39*). In the present study, we purified amphipol-reconstituted near full-length HER2, either alone or bound to full-length TZB, and analyzed them using cryo–electron microscopy (cryo-EM). The use of full-length proteins both for TZB and HER2 would potentially mimic the therapeutic interactions between the antibody and the receptor more closely than if only the Fab fragment or the ECD was used. Datasets of HER2 alone and in complex with TZB were then subjected to single-particle analysis (SPA). In the absence of the antibody, we obtained a conformation of HER2 similar to all previous studies. However, when analyzing HER2 bound to TZB, we identified a highly populated class distinct from the reported ones, with a "compact" conformation of the HER2 ECD head. We focused our structural analysis on this region because it harbors the dimerization arm-binding pocket, while the relative flexibility between the ECD head and subdomain IV–TZB limited the overall resolution of the HER2 ECD-TZB complex. The compact conformation is primarily characterized by a narrowing of the dimerization arm-binding pocket due to the approach of subdomains I and III, and it was not observed in the absence of the antibody. In this context, we propose that this pocket becomes so constricted that it would prevent a potential dimerization arm from another EGFR from binding. This result contributes to our current understanding of HER2 dynamics and the different mechanisms by which the widely used mAb TZB exerts its anticancer effect (*40*).

RESULTS

Structure determination of two conformations of the HER2-TZB complex

An engineered version of near full-length HER2 was used for the expression and purification of milligram amounts of the receptor. This construct carries a C-terminal truncation (Δ1008–1233) of the receptor to avoid the unstructured tail. Analogously to the HER1 construct used by Mi *et al.* (*41*, *42*), three point mutations were introduced in the kinase domain to replace surface cysteines with serines, to prevent disulfide bond formation: C789S, C805S, and C965S (fig. S1A). The purified HER2 was reconstituted into amphipols and studied by cryo-EM SPA both in the apo form and complexed with full-length TZB (fig. S1, B and C).

After several rounds of two-dimensional (2D) and 3D classifications, combined with 3D class consensus (*43*), several 3D density maps of the ECD of HER2 in complex with TZB were obtained ("TZB" dataset; Fig. 1, A and B, and fig. S2A). In the case of the TZB complex, only its Fab fragment was well resolved. In these maps, the ECD head of HER2 (composed of subdomains I-II-III) exhibited several degrees of bending with respect to the remaining complex,

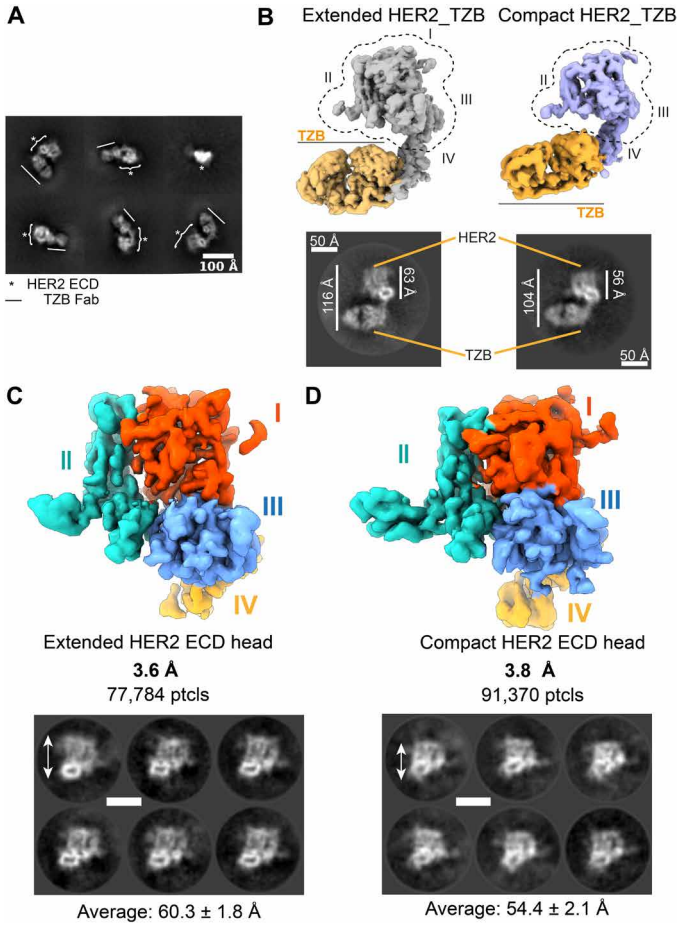

Fig. 1. Cryo-EM data processing of HER2-TZB dataset showing the extended and compact HER2 conformations in complex with TZB. (**A**) Representative 2D averages showing distinct secondary structure features of different views of the complex. Densities corresponding to the HER2 ECD or the Fab portion of TZB are labeled. Scale bar, 100 Å. (**B**) Top: Detail of two 3D classes representing two distinct conformations of the ECD in the HER2-TZB complex: extended (gray) and compact (purple). Dashed outline around the ECD head indicates the boundaries of the mask used for focused refinement in downstream steps. Density of TZB Fab is colored in light brown. For a more detailed workflow, refer to fig. S2. Bottom: 2D averages with particles (ptcls) filtered by angular assignment, such that only projections of "front views" were used in the average for each subset of particles. (**C**) Sharpened volume showing the extended conformation of HER2-TZB after focused refinement on the ECD head. (**D**) Sharpened volume of the compact HER2-TZB after increasing the number of particles of this conformation, followed by focused refinement on the ECD head. For clarity, density maps of the ECDs display subdomains in different colors. Subdomain I: From residues T23 to L215; subdomain II: T216 to C338; subdomain III: A339 to P500; subdomain IV: E501 to N629. Below each map, a collection of 2D averages of the ECD head after subtraction of the subdomain IV and TZB signal from each subset of particles, showing the average length of the ECD head (the measured distance is indicated with arrows). Scale bars, 50 Å.

namely, the subdomain IV of HER2 and the bound Fab region of TZB. This indicated a flexibility of the arrangement mediated by domain IV, a fact that has also been observed in previous studies with HER2 and other HERs using cryo-EM (*39*, *44*) and is therefore not per se unexpected.

However, in the TZB complex, the ECD head itself also seemed to present a varying degree of compaction among the 3D classes.

This is especially noticeable when comparing the class shown in gray in Fig. 1B, which presented an ECD head resembling the ones found in previous studies (*5*, *31*), with the one in purple, with the ECD head in a more compact structure. Differences between conformations were also present at the level of 2D classes, where both the height of the complex and of the ECD head in particular were shorter in the subset from the purple class, as shown in the 2D averages at the bottom of Fig. 1B.

Motivated by this qualitative observation, we decided to focus our image analysis and, consequently, alignment and map reconstruction efforts specifically on the ECD head, aiming at detecting more precisely potential changes in this region that harbors the dimerization arm-binding pocket. For terminology, we will refer to the gray class as the "extended class," to maintain the nomenclature given to HER2 ECD in previous studies where it adopted a similar conformation as other members of the EGFR family (*30*, *45*) and to the purple one as the "compact class."

To improve the density map of this putative compact conformation, template- and deep learning–based picking strategies, followed by extensive 3D classification, were combined to optimize the picking of receptor particles belonging to this conformation, going from 50,497 to 91,370 particles. Next, local refinement with a mask focused on the ECD head improved global resolution from 3.7 to 3.6 Å in the extended class and from 4.1 to 3.8 Å in the compact one (Fig. 1, C and D, and fig. S2, B and C) but at the expense of the resolution in the remaining part of the complex. This behavior implies that, despite the attempts to obtain homogeneous particle subsets via 3D classification, the relative movement between the ECD head and TZB (both connected by HER2 subdomain IV) prevents one from obtaining a better resolution across the complete 3D map. As anticipated from the 2D classes of the HER2-TZB complex, differences at the level of ECD alone can be appreciated with more detail after subtraction of the signal from subdomain IV–TZB (Fig. 1, C and D; average length: 60.3 versus 54.4 Å).

At this point, we turned to the study of the HER2 Apo structure, i.e., without TZB bound ("Apo" dataset), where we followed a similar processing pipeline as for the TZB dataset (fig. S3A). Next, the output Apo maps were then compared through correlation analysis of their head domains with the classes that were obtained in our previous analysis of the complex HER2-TZB [from Fig. 1 (C and D); correlations in fig. S3B]. In the Apo case, all maps presented a higher correlation with the extended conformation found in the HER2-TZB complex, clearly indicating that the Apo form was more similar to this extended conformation than to the compact one. Furthermore, in the final map of the Apo dataset (fig. S3C), the correlation with the map of the extended conformation was substantially higher than the correlation with the map of the compact conformation (0.830 versus 0.648).

Therefore, we conclude that the compact conformation of HER2 ECD could not be reliably found in a separate cryo-EM dataset of full-length HER2 in the absence of TZB, when a SPA procedure similar to that of the HER2-TZB dataset was applied. This finding therefore suggests that TZB induces, or at least stabilizes, the compact conformation. A comparison of the final Apo and TZB-bound extended and compact maps, as well as an extensive set of validation metrics, is shown in fig. S4.

It is important to note that validation metrics relative to map anisotropy demonstrate that the resolution is not uniform in all directions (fig. S4D), a common issue in cryo-EM when the particle distribution is not even throughout the ice layer. This effect is more visible in the two reconstructions from the TZB dataset with directions where the resolution drops up to 8 Å in the case of the compact reconstruction. Accordingly, we acknowledge that the 3D-FSC drops more abruptly in certain directions compared to the Apo dataset (fig. S4E). This behavior suggests that the addition of TZB has an effect on the particle orientation distribution, especially for the compact map. If anisotropy is strong, it might negatively affect data interpretability and particle alignment (an additional validation for the latter issue is presented in the next section). To prevent this, the compact map shown in Fig. 1D and fig. S2C was low-pass–filtered at 4.5 Å. We selected this value based on its Fourier shell occupancy (FSO) (fig. S4F) (*46*). This plot assesses the resolution at which a cryo-EM map starts becoming anisotropic. An FSO = 1 means that the map contains information in all directions at that resolution. In turn, as the FSO drops, the anisotropy of a map increases. At 4.5 Å, the FSO of the compact map is 0.75, which means that at this resolution, in at least 75% of orientations, the directional FSC is above the gold standard threshold of 0.143. Consequently, we also set this limit for downstream modeling (see Materials and Methods for more details).

All the analyses presented so far in this work are restricted to the HER2 ECD, despite working with the full-length protein. Beyond the ECD, flexibility in the juxtamembrane region of HER2 hindered the reconstruction of the full-length protein, which could only be resolved at low resolution, whether in amphipols or in nanodiscs (fig. S5). This outcome aligns with previous structural studies of EGFR family members (*30*, *44*) and cryo-EM structures of the insulin receptor and type 1 insulin-like growth factor receptor (*47*–*49*).

Structural differences between the compact and extended structures

To describe this previously unreported conformation in more detail and to compare it with already reported ones, atomic models of HER2 ECD were fitted and refined into both the extended and compact cryo-EM density maps from the TZB dataset (denoted "extHER2-TZB" and "compHER2-TZB" models from now on, respectively) and in the map derived from the complete Apo dataset (Apo model).

The three models obtained in the present study (Apo, extHER2-TZB, and compHER2-TZB; Table 1 and fig. S6A) were then compared with a set of other HER2 models already present in the Protein Data Bank (PDB), coming from both x-ray and cryo-EM studies. We find that virtually all structures are within 2-Å root mean square deviation (RMSD) from the Apo model (Fig. 2A) but with the clear exception of compHER2-TZB (RMSD >3.5 Å). Furthermore, when we measure the interdomain distance between centroids of subdomains I and III, compHER2-TZB also stands out as clearly different, presenting a substantially more compact structure (Fig. 2B).

A more detailed structural comparison is provided in Fig. 3. The models of Apo and extHER2-TZB can be superimposed with an RMSD of 1.102 Å (Fig. 3A), whereas the superposition of Apo or extHER2-TZB with compHER2-TZB produces an RMSD >3 Å. In general terms, we note that subdomain I and the upper half of subdomain II flex as a rigid body by around 15° toward the lower half of subdomain II and subdomain III in the compact conformation (Fig. 3B). This concerted movement does not affect all subdomains to the same extent. Specifically, subdomain II is the one showing the largest conformational change (RMSD = 2.972), followed by subdomain I (1.476) and, lastly, the subdomain III (1.331), which remains almost unchanged (Fig. 3C and movie S1).

Table 1. Cryo-EM processing and modeling statistics.

	HER2 Apo	extHER2-TZB	compHER2-TZB
	PDB ID: 9QBH	PDB ID: 9QBG	PDB ID: 9QBF
Data collection			
Microscope	Titan Krios G3i	Titan Krios G3i	Titan Krios G3i
Detector	Gatan K3	Gatan K3	Gatan K3
Energy filter slit width (eV)	20	20	20
Magnification	130,000	130,000	130,000
Voltage (kV)	300	300	300
Electron exposure (e^{-}/Å^2)	72.3	72.3	72.3
Defocus range (μm)	0.8–2.4	0.8–2.4	0.8–2.4
Pixel size (Å)	0.651	0.651	0.651
Symmetry imposed	C1	C1	C1
Number of micrographs	15,271	19,196	19,196
Initial particle images (no.)	5,437,963	4,207,722	4,207,722
Final particle images (no.)	364,430	77,784	91,370
Map resolution (Å)	3.8	3.6	3.8
FSC threshold	0.143	0.143	0.143
Sharpening B-factor (Å^2)	−172.59	−104.54	−123.10
Model refinement			
Number of atoms			
All (hydrogens)	7,687 (3,769)	7,687 (3,769)	7,631 (3,738)
Protein residues	508	508	504
Ligand (sugars)	0	0	0
Model validation			
CC (mask) map versus model (%)	0.77	0.74	0.65
CC (box) map versus model (%)	0.88	0.85	0.80
RMSD			
Bond lengths (Å)	0.021	0.021	0.024
Bond angles (°)	1.733	1.804	2.083
Ramachandran statistics			
Favored regions (%)	98.80	97.41	95.78
Allowed regions (%)	1.20	2.59	4.22
Outliers (%)	0	0	0
Rotamer outliers (%)	0	0	0
C-beta outliers (%)	0	0	0.22
Clashscore	1.30	1.43	4.06
MolProbity overall score	0.86	0.99	1.48

The refined cryo-EM map allowed us to model the interface between subdomains I, II, and III reliably at the subdomain level. The models show that the aperture of the dimerization arm-binding pocket is different in the two conformations. The magnitude of the conformational change is appreciated when comparing the Cα-Cα atom distances between pairs of amino acids located in opposite subdomains (Fig. 3, D and E). Residues that are well resolved in the cryo-EM maps were chosen as reference points. In this way, the interatomic distances between Q81 and T105 (both in subdomain I) to residues T312 and L313 (both in subdomain II) decrease from 13.7 and 15.0 to 11.3 and 10.7 Å, respectively. An even larger change is observed between Q106 (subdomain I) and R351 (subdomain III), where the distance decreases from 16.1 Å in the extended conformation to 9.1 Å in the compact form.

Last, a validation experiment was conducted to discard a potential model bias during map refinement. Low-pass–filtered versions of the extended or compact HER2 ECD maps were refined against the extended or the compact particle stack, as depicted in fig. S6B. Models from the output maps were compared, obtaining differences in RMSD of the same magnitude as in Fig. 3B, which implies that the structural information relative to the differences in conformation is contained in the experimental particle stack used for map refinement.

In summary, in the compact conformation, a narrowing of the dimerization arm-binding pocket occurs. This change is mediated

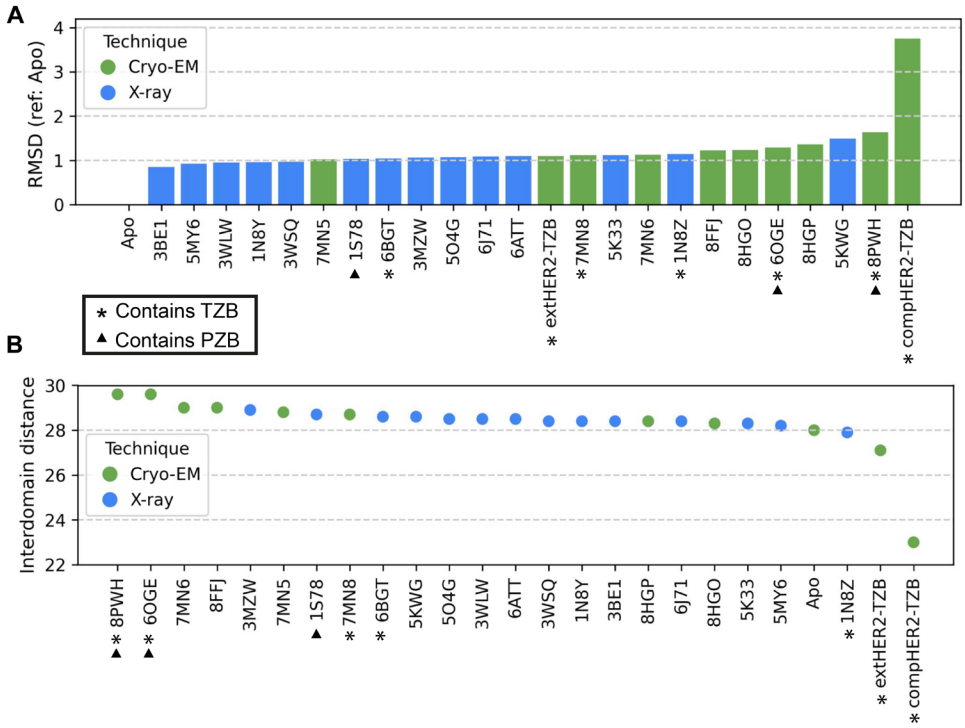

Fig. 2. Comparison of HER2 ECD models from this study with other HER2 models available in the PDB. (**A**) RMSD of models of HER2 available in PDB. As reference, we used the Apo model obtained from the Apo dataset in the present study (Fig. 3A). Only distances between pairs of Cα atoms were considered for RMSD calculation. (**B**) Interdomain distance in angstrom between centroids of subdomains I and III measured on models of HER2 available in the PDB and compared with those of the present work. The different models are identified with their PDB accession numbers. Colors indicate the experimental technique used to obtain the structures.

by the subdomain II, which bends such that its upper part and the whole subdomain I approach the subdomain III. This finding challenges the notion of the rigidity of the HER2 ECD while unveiling a previously undescribed effect of TZB on the ECD. This partial closure of the HER2 arm-binding pocket could hinder the ability of the HER3 dimerization arm to dock into it, potentially inhibiting the formation of the oncogenic unit.

Structural predictions of the inhibitory effects of TZB on HER2-HER3 heterodimerization

HER2 is known to form heterodimers with other EGFR family members, such as HER3 or HER1 (*1*), so we next explored how this compact conformation could affect the different heterodimer species that HER2 is able to form with HER3. TZB does not eliminate heterodimerization in the presence of a HER3 ligand (*38*, *50*). An atomic model of ligand-bound heterodimer in complex with TZB was obtained with cryo-EM recently (*30*), where HER2 displays an extended conformation. For ligand-independent heterodimerization, however, TZB shows an inhibitory effect on HER3 phosphorylation (*35*, *38*, *50*–*52*).

For these reasons, we explored whether a compact conformation of the HER2 ECD could engage in dimerization with a ligand-bound HER3. For that purpose, we used the experimental structure of HER2-HER3-NRG1β-TZB (*30*). The subdomain II of our compact structure was superimposed onto its equivalent in the HER2-HER3 heterodimer (Fig. 4A), mimicking the dimerization interface. In addition, unlike the structure with the extended conformation of HER2, numerous steric clashes are predicted to occur between the HER3 dimerization arm and the entrance of the HER2 dimerization arm-binding pocket (Fig. 4B). This suggests that the compact conformation of HER2, which is only found in complex with TZB, would hamper heterodimer formation with a liganded conformation of HER3. We describe the implications of an unliganded complex in the Discussion.

In the absence of ligand, HER3 predominantly adopts a tethered conformation, in which subdomain II bends toward subdomain IV in an autoinhibited configuration. Since there is no experimental report of a ligand-independent heterodimer structure, a model of a HER2-HER3 heterodimer was predicted using AlphaFold Multimer. Of the several predicted models, the one that exhibited the most reasonable monomer orientations within the dimer was selected (figs. S7A and S8A). We made this assessment based on 2D classifications of negatively stained EM images of the HER1 homodimer, where the orientations of the kinase domains are observed (*42*). The tethered HER3 ECD crystal structure (PDB 4LEO) and both of our HER2 cryo-EM structures (extended and compact) were then superimposed onto the AlphaFold Multimer–predicted structure (figs. S7, B to D, and S8, B to D). In the absence of TZB, no steric clashes between HER2 and HER3 were observed (figs. S7, C and E, and S8, C and E). However, in the presence of TZB, the two models, containing either the extended or the compact HER2 ECD, show considerable clashes between the TZB moiety and the tethered form of HER3 (figs. S7, D and E, and S8, D and E), anticipating a steric hindrance in the HER2-HER3 association when HER3 adopts its tethered conformation, regardless of the conformation of HER2 ECD.

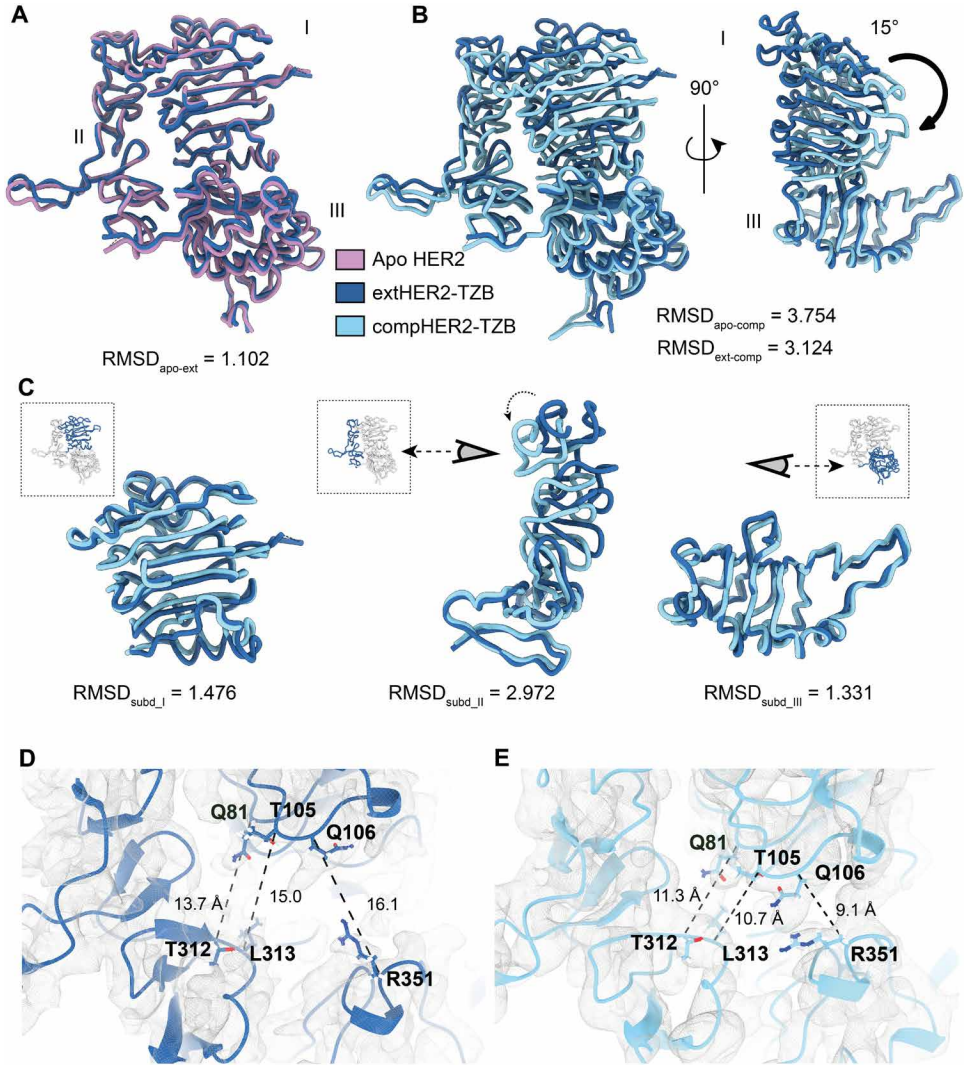

Fig. 3. Comparison of atomic models of the two conformations of the HER2-TZB complex. (**A**) Overlay of backbones of atomic models of Apo and extHER2 ECDs. For RMSD, the Apo model was used as a reference. (**B**) Overlay of backbones of atomic models of extended and compact TZB-bound HER2 ECDs, aligned on subdomain III. Left: Front view. Right: Side view (subdomain II is hidden for clarity). For RMSD, either the Apo or the extHER2 model was used as a reference, as indicated by the subscript. (**C**) Comparison of individual subdomains of extHER2-TZB and compHER2-TZB. Insets show the subdomain being compared and the direction of view. Left: Subdomain I. Middle: Subdomain II. Right: Subdomain III. For RMSD, the extHER2-TZB model was used as a reference. (**D** and **E**). Cα-Cα distance between pairs of selected residues from subdomains I, II, and III at the crevice in the extended and compact models, respectively.

DISCUSSION

HER2 ECD exhibits conformational variability upon TZB binding

The present work explores the influence of TZB (the full antibody) on the ECD head of monomeric HER2 using a near full-length construct (instead of the ECD only) in solution by cryo-EM. In particular, it focuses on the flexibility of the ECD head (composed of subdomains I to III).

This is not the first time that flexibility of the HER2 receptor (Apo or TZB bound) has been addressed, either experimentally or with molecular dynamics (*37*, *39*, *53*), although all previous studies were using constructs of the ECD only. However, these studies have focused their research on characterizing the flexibility of the TZB-bound subdomain IV relative to the ECD head via a hinge movement at the interface of subdomains III and IV (*39*). Other authors have even suggested contacts between the Fab and subdomains II and III in molecular dynamic simulations (*37*, *54*). In line with these findings, we observed a similar behavior in SPA, where the subdomain IV oscillates from an almost perpendicular position with respect to the ECD head to a totally bent pose, with TZB apparently in contact with the ECD head (fig. S1A, right).

However, the potential rearrangements occurring within the ECD head upon TZB binding, which could affect the dimerization arm-binding pocket, had not been deeply explored so far. In this work, we present three structures of HER2 ECD, two of them are very similar to those already described (Apo and extHER2-TZB; fig. S3C and Fig. 1C) and a so far unobserved one, where the ECD head undergoes a compaction that moves subdomain I closer to subdomain III, mediated by the subdomain II (Fig. 1D). Molecular dynamic simulations conducted by Fuentes *et al.* (*54*) with HER2-TZB complex reported that fluctuations in subdomain II increase when TZB binds.

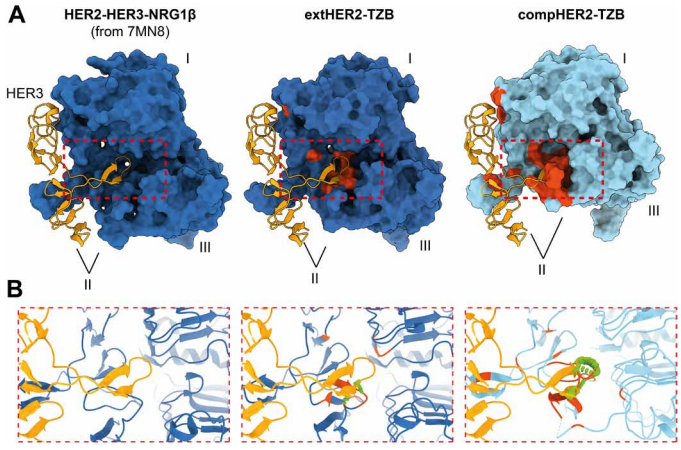

Fig. 4. Superposition of the monomeric compact and extended conformations of the HER2 ECD-TZB complex on the cryo-EM HER2-HER3-NRG1β-TZB complex. (**A**) Dimerization interface of several HER2 ECD models interacting with the HER3 dimerization arm. The specific HER2 model used in the figure is indicated in the text above it; in all cases, models were aligned on subdomain II, to visualize a hypothetical position of the HER3 dimerization arm in the dimerization arm-binding pocket. In orange, ribbon depiction of HER3 subdomain II. In dark blue, surface representation of the HER2 ECD head as it is in the model from the study of Diwanji *et al.* (*30*) (left) and after being substituted by the extHER2-TZB model (middle). In cyan, the HER2 model from (*30*) was substituted by the compHER2-TZB model (right) from this study. Residues with steric clashes are highlighted in red. (**B**) Detail of the dimerization arm-binding pockets from the insets in (A), with HER2 in ribbon depiction. In red, residues of HER2 involved in steric clashes. For clarity, only clashes between backbone atoms are displayed (dashed lines in light green).

To highlight how different this previously undescribed compact conformation was, we compared our models with those already published. Structures of HER2 and HER2-TZB have been obtained before, using x-ray crystallography with constructs comprising the ECD only (*5*). In these cases, the interdomain distance, measured as the distance between centroids of subdomains I and III (see Materials and Methods for more details) was similar, being 28.4 (PDB 1N8Y) and 27.9 (1N8Z) Å, respectively (Table 2 and Fig. 2B). The interdomain distance in our Apo and extHER2 ECD models reported in this work is also similar to the previous cases, being 28.0 and 27.1 Å, respectively. In both cases, the unbound HER2 presents a slightly larger interdomain distance than the extended TZB-bound structure, although this difference is not enough to ascertain that they constitute distinct conformations, especially when their RMSD is around 1 Å. In other HER2 x-ray studies performed so far with monomeric HER2 in complex with different binding macromolecules (affibodies, nanobodies, and antibodies), the interdomain distance ranges from 27.9 to 28.9 Å (*55*–*59*).

However, the interdomain distance in the compact model (compHER2-TZB, 23.0 Å) is the shortest reported so far. Likewise, its RMSD (3.8 Å; Fig. 2A), measured against the Apo model, confirms that it is the most distinct conformation of all the HER2 models considered in this analysis. The use of truncated constructs and limitations of the x-ray technique, where only the most prone-to-crystallization conformation can be solved, could explain why this conformation has remained elusive in the past, although it is highly populated in our sample.

Other structural studies including HER2-TZB have been carried out before in solution with cryo-EM. However, they all included at least a third protein bound to HER2 in the complex: HER1 (*60*), HER3 (*30*), HER4 (*45*), or PZB (*31*, *39*). This could have potentially precluded the detection of a compact-like confirmation due to steric clashes with other HER monomers or reduced the mobility in the ECD head induced by PZB (epitope in subdomain II). The longest interdomain distance was measured in complexes containing PZB (29.6 Å in 6OGE and 8PWH).

The structural differences of the compact conformation are also noticeable on the basis of the relative rotation of the subdomain III. Figure S9A shows a comparison of a set of HER2 structures with a variety of interacting partners. The largest rotation is observed in the compact conformation bound to TZB. In contrast, HER2 remains in its extended conformation when bound to other partners in interactions that involve the subdomain II. The comparison also reveals a slightly more extended ECD in the HER2-PZB-TZB complex.

Together, this study and its comparison with other structures published elsewhere demonstrate that the HER2 ECD head is more flexible than traditionally regarded, being able to adopt a range of conformational changes as a function of the binding partner. This work expands the spectrum of conformations and contributes with the most compact conformation reported so far.

Implications of the HER2 compact conformation in the HER2-HER3 heterodimer

Recently, Diwanji *et al.* (*30*) proposed a correlation between the degree of opening of the dimerization arm-binding pocket upon ligand binding and the engagement of the dimerization arm from the opposite monomer. They described a spectrum of states, ranging from a closed dimerization arm-binding pocket, where the ligand is fully wedged by subdomains I and III (as is the case for HER1 and HER3 with ligands EGF and NRG1β, respectively) (fig. S9B); a partially closed dimerization arm-binding pocket [induced by epiregulin (EREG), which is partially wedged by HER1]; and an open pocket, as it occurs for nonwedged orphan HER2. This opening of the dimerization arm-binding pocket would be responsible for the dynamic nature of the HER3 dimerization arm and thus its ability to bind to HER2. The dimerization arm was resolved only in complex with the oncogenic S310F HER2 mutant, which fixes the HER3 dimerization arm and with NRG1β complexed to HER3. Otherwise, in wild-type HER2, this dimerization arm of HER3 interacts dynamically with the HER2 arm-binding pocket and may not seem essential for heterodimerization (*30*).

The compact conformation of HER2 described here adds a previously undescribed point to the spectrum of ECD conformations found in the EGFR family, which can be compared on the basis of its arm-binding pocket opening and interdomain distance. In this context, compHER2-TZB subdomain III presents a rotation somewhere in between the partially and not wedged structures (fig. S9B, right). At the same time, its interdomain distance is the shortest among the HERs structures (fig. S9C). Together, these changes reduce the accessibility of potential partners to the arm-binding pocket. The possible functional implications in dimerization are discussed here, using the HER2-HER3 heterodimer as an example. A superposition of the extHER2 and compHER2 models on the dimerization interface of the HER2-HER3 heterodimer (Fig. 4, A and B) anticipates steric clashes in the HER2 dimerization arm-binding pocket, especially severe for the compact conformation.

We hypothesize that a narrower pocket would negatively affect the engagement of the HER3 dimerization arm. These contacts

Table 2. Comparison of Apo, extHER2-TZB, and compHER2-TZB models with other HER2 models.

PDB	Technique	Construct	Binder	Centroid_ subdomain_I-III (Å)	RMSD (Å)
compHER2-TZB	Cryo-EM	Near FL*	TZB	23.0	3.754
extHER2-TZB	Cryo-EM	Near FL*	TZB	27.1	1.102
1N8Z	X-ray	ECD	TZB	27.9	1.139
Apo	Cryo-EM	Near FL*	Apo	28.0	0.0
5MY6	X-ray	ECD	Nb	28.2	0.920
5K33	X-ray	ECD	Fcab	28.3	1.116
8HGO	Cryo-EM	ECD	HER1-EGF	28.3	1.231
6J71	X-ray	ECD	hAb	28.4	1.086
8HGP	Cryo-EM	ECD	HER1-EREG	28.4	1.365
3BE1	X-ray	ECD	bH1Fab	28.4	0.855
1N8Y	X-ray	ECD	Apo	28.4	0.961
3WSQ	X-ray	ECD	Fab/HER2	28.4	0.972
6ATT	X-ray	ECD	BiparatopicAb	28.5	1.094
3WLW	X-ray	ECD	Fab/HER2	28.5	0.949
5O4G	X-ray	ECD	Fab/HER2	28.5	1.071
5KWG	X-ray	ECD	Fcab	28.6	1.489
6BGT	X-ray	ECD	mtTZB	28.6	1.043
7MN8	Cryo-EM	Near FL*	TZB/HER3	28.7	1.115
1S78	X-ray	ECD	PZB	28.7	1.034
7MN5	Cryo-EM	Near FL*	HER3	28.8	1.025
3MZW	X-ray	ECD	Affibody	28.9	1.057
8FFJ	Cryo-EM	ECD	Zamidatumab	29.0	1.225
7MN6	Cryo-EM	Near FL*	HER3	29.0	1.123
6OGE	Cryo-EM	ECD	PZB-TZB	29.6	1.289
8PWH	Cryo-EM	ECD	PZB-TZB	29.6	1.634

*Near full-length construct, with a truncation of the disordered C-terminal tail.

would force the dimerization arm of HER3 to adopt a presumably less energetically favorable position that could hinder, or even prevent, the interaction at the dimerization interface with a hypothetical transient, extended-like ligand-less HER3.

Therefore, our results contribute to a conceptual model that may explain the differential effect of TZB on HER3 phosphorylation, depending on the presence of HER3 ligands (*38*). In every case, for phosphorylation to occur, the kinase domains must be within dimerization distance of each other, thus requiring the ECD to also be within the dimerization distance of each other, even if they are not tightly interacting. Conformational variation has been observed in cryo-EM structures of EGFR homodimers (*44*, *61*); it is thus very well possible that also HER3 is not necessarily in a permanently tethered conformation when not liganded. When bound to an antibody such as LJM716, which traps HER3 in an inactive state, phosphorylation of HER3 is inhibited even when HER2 is overexpressed (*62*). However, when the receptor is not bound to such an antibody, phosphorylation of HER3 occurs when HER2 is overexpressed, even in the absence of ligand (*38*). It is therefore plausible that HER3 may exhibit a variety of conformational states in the absence of ligand. Some of these states may be partially active, albeit present in insufficient quantities for any detectable association with HER2 at its normal expression level. However, upon overexpression of HER2 as in aggressive tumors, such partially active states of HER3 could have a larger probability of interacting with the HER2 ECD, in turn shifting the conformational equilibrium of HER3, and eventually stabilizing a fully active conformation in the heterodimer, even in the absence of HER3 ligands.

Ligand-free HER3 is expected to interact more weakly with HER2, compared to the ligand-bound HER3. In this context, the narrower binding pocket in compact HER2 may be sufficient to weaken the interaction between the receptors in a similar albeit weaker way as described in Fig. 4 for the ligand-bound heterodimer. However, in a case where HER3 associates with overexpressed HER2 while in a tethered conformation rather than a transiently active one, TZB would obstruct the HER2-HER3 interaction via steric clashes. This would constitute a dual inhibitory effect of TZB on ligand-independent heterodimerization: on the one hand, steric clashes of HER3 with the TZB itself and, on the other hand, steric clashes of the HER3 dimerization arm with the narrowed dimerization arm-binding pocket of HER2. Thus, TZB is expected to diminish HER3 phosphorylation in the absence of HER3 ligand, consistent with a pivotal study by Junttila *et al.* (*38*).

In contrast, in the presence of a HER3 ligand, the interaction between the HER3 and HER2 ECDs is stabilized (*30*), leading to the clash between TZB and HER3 being alleviated by adaptation within HER2, such that TZB is no longer a sufficiently strong inhibitor.

Again, this is consistent with the lack of signaling inhibitory effect by TZB in the presence of HER3 ligand (*38*).

Another factor contributing to the influence of dimerization by TZB has been proposed by Ruedas *et al.* (*39*), in that the loop 581-590 may be closer to the corresponding loop of HER3 in the HER2-HER3 complex, although this is not well resolved, and somewhat further away in the HER2-HER3-TZB complex (*30*, *39*). This study, however, did not consider the contribution of the dimerization loop.

Besides investigations on the inhibition of signaling, previous studies have already examined the effect of TZB on HER2-HER3 heterodimer formation in experiments with cancer cell lines that overexpress HER2 (SKBR3 and BT474-M1) (*38*). When immunoprecipitating HER2, HER3 was coimmunoprecipitated in the absence of antibodies, but this was greatly diminished in the presence of TZB and PZB, which binds to the HER2 dimerization arm in subdomain II (*63*). In contrast, in the presence of the ligand heregulin, TZB lost its ability to diminish HER3 coimmunoprecipitation, while PZB maintained it. These coimmunoprecipitation data correlated well with the phosphorylation of HER3: Both TZB and PZB inhibit it in the absence of heregulin (TZB even more strongly), while addition of heregulin leads to a strong increase of pHER3. Other experiments have directly measured HER2-HER3 heterodimerization in HER2-overexpressing SKOV-3 cells with time-resolved Förster resonance energy transfer (FRET), using antibodies that bind to epitopes not involved in the interaction (*64*). These experiments directly showed an inhibitory effect of TZB on HER2-HER3 heterodimer formation in the absence of a ligand.

In summary, our structural results propose a mechanism as to why TZB may only have a minor inhibitory effect in ligand-dependent HER2-HER3 heterodimers while exerting a substantial effect in ligand-independent HER2-HER3 heterodimerization. The fact that only a limited fraction of the HER2-TZB particles is in the compact conformation (Fig. 1A) would explain why the presence of TZB is not enough by itself to prevent ligand-dependent heterodimerization. Further experimental evidence will be required to support this hypothesis. To produce desirable therapeutic effects, a valuable goal would be to target the ligand-binding pocket more specifically, so as to mimic the compact conformation in a more efficient manner than TZB does. This would be particularly interesting in S310F mutant HER2, which stabilizes the interaction with the dimerization arm of HER3. Such a molecule might act synergistically with PZB, which targets the dimerization arm of HER2, and could also form the basis of an ADC with multiple modes of action. Nonetheless, additional work is needed to fully characterize the molecular mechanism of the effect of TZB on HER2 ECD and its consequences on its heterodimerization capabilities. Together, the present work constitutes an important contribution to our understanding of the dynamics of the HER2 receptor.

MATERIALS AND METHODS

Experimental design

The objective of the study was to gain insights into the structural effects of full-length TZB on the near full-length HER2 receptor, particularly on its ECD head, composed of subdomains I, II, and III. For that purpose, cryo-EM datasets of HER2, either alone or in complex with TZB, were collected, analyzed, and compared, with the aim of revealing structural differences that could be attributed to the binding of the mAb.

Expression of HER2

The HER2 construct used was cloned into a modified pFL vector (MultiBac system, Geneva Biotech), resulting in an expression construct with an N-terminal melittin signal sequence, followed by a FLAG-tag, a His_{10}-tag, a human rhinovirus 3C protease cleavage site, and an hemagglutinin (HA)–tag. Following the HA-tag was the sequence of native human HER2 (Gene name: *ERBB2*; UniProt: P04626-1) with an N-terminal truncation of its native signal sequence (Δ1–22) and a C-terminal truncation (Δ1030–1255) which is directly followed by a human rhinovirus 3C protease cleavage site and the superfolder Green Fluorescent Protein (sfGFP) sequence. Three point mutations in the HER2 kinase domain (C789S, C805S, and C965S) were also introduced (fig. S1A).

The expression cassette was integrated into the DH10EMBacY baculovirus genome, and the resulting bacmid was transfected into *Sf9* insect cells in six-well tissue culture plates (2 ml of cell suspension at a density of 4×10^5 cells/ml) using 8 μl of Cellfectin II Reagent (Thermo Fisher Scientific) and 200 μl of Sf-900 II serum-free medium (SFM) (Thermo Fisher Scientific). After a 5-hour incubation in a humidified 27°C incubator, the transfection medium was replaced by 2 ml of SF-900 II SFM supplemented with 1% (v/v) penicillin-streptomycin solution (100 ml; Sigma-Aldrich, P0781). After a 5-day incubation, viral V0 stocks were harvested and subsequently amplified to obtain viral V1 stocks by adding 20 μl of V0 stocks to 50 ml of cell suspension (cell density, 1×10^6 cells/ml) in SF-900 II SFM supplemented with 1% (v/v) penicillin-streptomycin solution. After a 72-hour incubation at 27°C under constant shaking, the viral V1 stocks were harvested by centrifugation at 7000*g* for 10 min at 4°C. V1 stocks were further amplified to obtain high-titer viral V2 stocks by adding 125 μl of V1 stocks to 250 ml of cell suspension (density, 1×10^6 cells/ml) in SF-900 II SFM supplemented with 1% (v/v) penicillin-streptomycin solution. After a 72-hour incubation at 27°C under constant shaking, the viral V2 stocks were harvested by centrifugation at 7000*g* for 10 min at 4°C.

For expression, 5 liters of *Sf9* insect cells in SF-900 II SFM medium supplemented with 1% (v/v) penicillin-streptomycin was infected with V2 virus at a cell density of 4×10^6 cells/ml and a multiplicity of infection of 5. After a 72-hour incubation at 27°C under constant shaking, the cells were harvested by centrifugation at 1200*g* for 10 min at 4°C. The cells were washed with phosphate-buffered saline, frozen in liquid nitrogen, and stored at −80°C.

Purification of HER2

Insect cells expressing the human HER2 construct were lysed by sonication on ice for 15 min using a Sonifier 250 (Branson) at a duty cycle of 30% and output 5, with a 3-min cooldown after 1 min of sonification. Receptor-containing membranes were then isolated by repeated Dounce homogenization in hypotonic buffer [10 mM Hepes (pH 7.5), 20 mM KCl, 10 mM $MgCl_2$, Pefabloc SC (0.1 mg/ml; Roche), and pepstatin A (2 μg/ml; Carl Roth)], followed by hypertonic buffer [10 mM Hepes (pH 7.5), 20 mM KCl, 10 mM $MgCl_2$, 1.0 M NaCl, Pefabloc SC (0.1 mg/ml; Roche), and pepstatin A (2 μg/ml; Carl Roth)] in the presence of 10 μM lapatinib (Cayman Chemical, Cay11493) and deoxyribonuclease I (DNase I; 90 μg/ml; Roche). Washed membranes were collected by ultracentrifugation at 95,800*g* for 30 min at 4°C. Purified membranes were then resuspended in hypotonic buffer in the presence of 20 μM lapatinib and DNase I (90 μg/ml) and then incubated for 2 hours at 4°C while turning on a wheel. The receptor was subsequently extracted from the membrane by

incubating with solubilization buffer [12 mM Hepes (pH 7.5), 800 mM NaCl, and 0.5% (w/v) Fos-choline-16 (FC16; Anatrace)] at 4°C for 5 hours. Insoluble material was removed by centrifugation at 95,800*g* for 30 min at 4°C. The supernatant was incubated with TALON IMAC resin (Cytiva) at 4°C overnight to bind the receptor to the resin.

The receptor-bound resin was washed with 20 column volumes (CVs) of wash buffer I [50 mM Hepes (pH 7.5), 800 mM NaCl, 10 mM $MgCl_2$, 8 μM lapatinib, 25 mM imidazole, 10% (v/v) glycerol, and 0.05% (w/v) FC16], followed by 20 CVs of wash buffer II [50 mM Hepes (pH 7.5), 600 mM NaCl, 1 μM lapatinib, 25 mM imidazole, and 0.0016% (w/v) FC16]. The receptor was then eluted stepwise with 3 CVs of elution buffer [50 mM Hepes (pH 7.5), 400 mM NaCl, 1 μM lapatinib, 250 mM imidazole, and 0.0016% (w/v) FC16]. The protein was concentrated to ~1 to 2 mg/ml using a 100-kDa molecular weight cutoff Vivaspin 20 concentrator (Sartorius Stedim).

Reconstitution in amphipols and HER2-TZB complex formation

The purified HER2 construct at ~1 to 2 mg/ml was mixed with Amphipol A8-35 (Anatrace) in a 1:50 molar ratio in a maximum volume of 200 μl and incubated for 30 min with shaking at 4°C. BioBeads SM-2 resin (Bio-Rad) were added to the mix (50%, v/v) and incubated for 16 hours with shaking at 4°C, after which the BioBeads were removed. Up to 10 × 200 μl reconstitution mixtures were prepared and combined after the 16-hour incubation with BioBeads. The HER2-amphipol mix was centrifuged at 22,000*g* at for 5 min at 4°C. The supernatant was then fractionated on a Superose 6 Increase 10/300 GL (Cytiva) equilibrated with gel filtration buffer [40 mM tris-Cl (pH 7.5) and 300 mM NaCl].

For the formation of the HER2-TZB complex, the purified receptor was first mixed with TZB (Hölzel-Diagnostika) in a 1:3 (HER2:TZB) molar ratio. The mixture was incubated overnight at 4°C while turning on a wheel. The mixture was subsequently centrifuged at 22,000*g* for 5 min at 4°C and then fractionated on a Superose 6 Increase 10/300 GL equilibrated with gel filtration buffer.

Sample preparation of cryo-EM and image acquisition

For cryo-EM grid preparation, 3 μl of purified amphipol-reconstituted HER2-TZB complex was applied on glow-discharged holey carbon gold grids (200 mesh, R 1.2/1.3; Quantifoil) and subsequently vitrified using a Vitrobot Mark IV (Thermo Fisher Scientific) operated at 100% humidity and 4°C. Cryo-EM images were acquired on a Titan Krios G3i (Thermo Fisher Scientific), operated at 300 kV, at a nominal magnification of 130,000 using a K3 direct electron detector (Gatan) in super-resolution mode, corresponding to a pixel size of 0.325 Å. A BioQuantum energy filter (Gatan) was operated with an energy slit width of 20 eV. A total of 24,624 movies were obtained, with an exposure rate of ~25.5 electrons/pixel per second and a defocus range of −0.8 to −2.4 μm using automatic data acquisition with the EPU software (Thermo Fisher Scientific). The total exposure time was 1.2 s with an accumulated dose of ~72.3 electrons/$Å^2$ and a total of 89 frames per micrograph, dose-fractionated to 45 fractions.

The same conditions and parameters were also applied for the data collection of amphipol-reconstituted HER2 in the absence of TZB (first set collected 11,360 movies and second set with 27,148 movies), for the purified HER2 reconstituted into MSP1D1ΔH5-based nanodiscs (10,116 movies), and for the purified HER2 reconstituted into nanodiscs produced with saposin A (8750 movies). See Supplementary Methods for nanodisc preparation.

Cryo-EM data processing

HER2-TZB dataset (TZB dataset)

Raw movies were binned to generate a pixel size of 0.65 Å, followed by motion correction and dose weighting using MotionCor2 (*65*). A total of 19,196 aligned micrographs were imported into Scipion (*66*) for further processing inside this platform. Contrast Transfer Function (CTF) estimations from Ctffind4 (*67*) and "xmipp - ctf estimation" were compared through "xmipp - ctf consensus" (*43*) for micrograph curation based on resolution, defocus, astigmatism, and ice thickness, yielding a subset of 16,521 micrographs for further analysis. A total of 4,207,722 coordinates were initially picked with crYOLO (*68*). Particles were extracted at a sampling rate of 3.91 Å/pixel and were subjected to several rounds of 2D classifications and ab initio reconstructions with posterior 3D heterogeneous refinements in eight classes with cryoSPARC (*69*) to further clean the particle set. Particles (483,064) from output classes that reached Nyquist resolution were reextracted at 1.302 Å/pixel and 300 pixel box size, followed by two parallel 3D heterogeneous refinement runs. Output classes from these two classifications were compared with the "xmipp - consensus clustering 3D" protocol (*43*) to find subsets of particles that remained together in two independent runs.

The top five most populated subsets of this consensus were then refined with cryoSPARC nonuniform refinement (*70*), masking the densities of HER2 ECD and Fab from TZB and excluding the remaining noisy densities of the antibody. At this stage, classes corresponding to the extended (77,784 particles; Fig. 1A) and compact (50,497 particles; Fig. 1A) conformations were identified.

To increase the number of particles of the compact conformation, projections of a map in this conformation were used to pick particles with gautomatch (*71*), resulting in 2,757,666 coordinates. Particles were classified following the same workflow described above and merged with other existing subsets of particles enriched in the compact conformation, removing duplicates and gathering a total of 191,934 particles. At this stage, particles were windowed to 200 pixels and subjected to additional rounds of 2D and 3D heterogeneous refinements and consensus clustering 3D. The final particle subset of particles (91,370) in the compact conformation was subjected to another round of nonuniform refinement. The gold standard FSC reported a global resolution of 4.1 Å. A final round of focused refinement with mask on the ECD head was run with cryoSPARC local refinement for the extHER2-TZB and compHER2-TZB particles for the final resolutions of 3.6 and 3.8 Å, respectively.

HER2 without TZB (Apo dataset)

The dataset corresponding to HER2 in the absence of TZB was analyzed following an essentially identical workflow as for the HER2-TZB dataset: All image stacks were binned to generate a pixel size of 0.65 Å followed by motion correction and dose weighting using MotionCor2 (*65*). A curated set of 15,271 micrographs was picked with crYOLO. A set of 5,437,963 particles at 2.44 Å/pixel and 80 pixel box size was subjected to several rounds of 2D classifications with cryoSPARC, reducing the number of particles to 2,387,638. Then, several rounds of 3D heterogeneous refinement were carried out, keeping only classes that resembled ECDs of HER2, ending with 547,685 particles. At this point, particles were reextracted at 1.302 Å/pixel in a 250 pixel box size and subjected to two independent 3D heterogeneous refinement runs (eight classes), followed by a consensus 3D clustering. The top 10 most populated subsets of particles from the 3D consensus underwent nonuniform refinement and sharpening with deepEMhancer (*72*).

The set of 547,685 particles was subjected to the following workflow: windowing to 200 pixels, followed by an angular consensus, keeping particles whose angular assignments disagree no more than 4° after two independent nonuniform refinement runs for a final number of 364,430 particles. Next, local refinement with a mask focused on the ECD head yielded a final map at a resolution of 3.8 Å.

All the refined maps (from Apo and TZB datasets) were sharpened with RELION-5 Postprocessing (*73*) or deepEMhancer. Global resolution was calculated following the gold standard FSC at 0.143, and local resolution maps were estimated using MonoRes (*74*). 3D-FSC, FSO, and directional resolution plots were calculated with "xmipp - resolution fso" (*46*).

HER2 in saposin A discs and HER2 in MSP nanodiscs

Both datasets were processed similarly as described above, giving as a result maps of truncated HER2 showing the ECD only (fig. S5, A and B). The workflow to obtain low-resolution near full-length HER2 maps, with the saposin A dataset (7291 movies) as an example, was as follows: A set of coordinates of saposin discs (300,410) was merged to a set of coordinates that yielded a high-resolution ECD map (74,457). Using the protocol "xmipp - picking consensus," we selected pairs of coordinates within a distance compatible with the receptor being embedded in the disc (150 Å). For each pair fulfilling this condition, the new coordinate of the presumably disc-associated HER2 was at the midpoint between the coordinates of the pair members. A total of 26,655 particles met this condition and were subjected to 2D classification with cryoSPARC, obtaining a gallery of 2D averages with blurry density under the ECD (fig. S5C). These averages were used as templates for picking with gautomatch. After consecutive rounds of 2D classifications with cryoSPARC and 3D classifications with RELION-5 (*73*), with a *T* value of 10, a low-resolution map displaying the ECD with extra densities below was obtained (fig. S5, D and E).

Model building and refinement

The high-resolution crystal structure of HER2 chain in PDB 5MY6 was used as the starting model to dock into the cryo-EM maps. Overall, similar procedures were followed for atomic model refinements against Apo HER2, extHER2-TZB, and compHER2-TZB reconstructions. The structure was initially relaxed with all-heavy-atoms constraints before refining it into the full map using Rosetta. Rigid-body fitting of relaxed models into the cryo-EM maps was performed in Chimera v1.15 (*75*). The starting model was subjected to a first round of refinement against the full map with the Rosetta Relax protocol (*76*). The density map was assigned a scoring function weight of 35.0, with a resolution limit of 4.5 Å. Output models were then re-refined against the full map in Phenix, maintaining the same resolution limit. Secondary structure restraints were calculated from the starting crystal structures, using phenix.secondary_structure_restraints as implemented in Phenix v1.20.1-4487 (*77*). These extra restraints were included in the first real-space refinement cycles with Phenix, using also Ramachandran restraints (*77*) with global minimization, with simulated annealing and Atomic Displacement Parameters (ADP) options enabled. The output model was subjected to an additional round of refinement against the full map with Rosetta Relax. Further fitting of Ramachandran and other geometry outliers was done with Coot v0.9.8.95 (*78*), using also full maps sharpened with RELION-5 Postprocessing protocol or deepEMhancer. Model validation was performed continuously within Coot and Phenix against the full map. Per-residue and average *Q* score metrics (*79*) were calculated with MapQ (v2.9.7; https://github.com/gregdp/mapq). The resolution parameters for atomic *Q* score calculation in Apo, extHER2-TZB, and compHER2-TZB were 3.8, 3.6, and 4.5 Å, respectively, with a default sigma of 0.4. Per-residue resolution values were derived from per-residue *Q* scores by solving the third-order regression equation that relates *Q* score to map resolution in MapQ.

Structural analyses

Volume and model illustrations were created using ChimeraX (*75*), as well as alignment of models and Cα-Cα distance measurements. RMSDs were calculated with the "matchmaker" tool in ChimeraX, considering only Cα-Cα distances between pairs of residues being aligned. Relative intersubdomain rotation was calculated by measuring the angle formed by axes fitted in the subdomains under study with the "define axis" tool in ChimeraX. For interdomain distances, residues from Q24-D118 and L137-L161 were considered to calculate the centroid of the subdomain I (excluding the flexible loop and the upper part of subdomain I due to poorer resolution in this region), and residues from K368-L377 and Q393-P500 were considered to calculate for the centroid of subdomain III (excluding a flexible loop to avoid contribution of local differences). Residues in equivalent positions were considered for centroid calculation in models of other HER family members.

For the 2D classes of the extended and compact conformations shown in Fig. 1B, front views were obtained as follows: A 3D reconstruction of the compact HER2-TZB was aligned to a map of the extended conformation. The transformation matrix calculated for the alignment was then applied to the compact particles accordingly using the "xmipp - align volumes and particles" protocol. Next, particles were filtered on the basis of their tilt and rot angles, obtaining ∼1000 particles of each conformation and averaged with a 2D classification protocol with cryoSPARC.

Measurements of ECD head length on 2D averages (Fig. 1, C and D) was done as follows: The signal from subdomain IV and TZB Fab was subtracted from the raw particles with the "xmipp - subtract projection" protocol (*80*). A locally refined map focused on the subdomain IV–TZB subregion of HER2-TZB was used as a projection reference. Subtracted particles were subjected to 2D classification in RELION-5 (*73*), with a $T = 10$. Averages presenting a clear front view of the ECD were binarized with automatic thresholding with ImageJ to obtain uniform measurements.

Supplementary Materials

The PDF file includes:

Supplementary Methods
Figs. S1 to S9
Legend for movie S1
References

Other Supplementary Material for this manuscript includes the following:

Movie S1

REFERENCES AND NOTES

1. Y. Yarden, M. X. Sliwkowski, Untangling the ErbB signalling network. *Nat. Rev. Mol. Cell Biol.* **2**, 127–137 (2001).
2. M. A. Olayioye, R. M. Neve, H. A. Lane, N. E. Hynes, The ErbB signaling network: Receptor heterodimerization in development and cancer. *EMBO J.* **19**, 3159–3167 (2000).
3. A. Arkhipov, Y. Shan, E. T. Kim, R. O. Dror, D. E. Shaw, Her2 activation mechanism reflects evolutionary preservation of asymmetric ectodomain dimers in the human EGFR family. *eLife* **2**, e00708 (2013).
4. C. Jost, J. C. Stüber, A. Honegger, Y. Wu, A. Batyuk, A. Plückthun, Rigidity of the extracellular part of HER2: Evidence from engineering subdomain interfaces and shared-helix DARPin-DARPin fusions. *Protein Sci.* **26**, 1796–1806 (2017).

5. H. S. Cho, K. Mason, K. X. Ramyar, A. M. Stanley, S. B. Gabelli, D. W. Denney Jr., D. J. Leahy, Structure of the extracellular region of HER2 alone and in complex with the Herceptin Fab. *Nature* **421**, 756–760 (2003).
6. D. Graus-Porta, R. R. Beerli, J. M. Daly, N. E. Hynes, ErbB-2, the preferred heterodimerization partner of all ErbB receptors, is a mediator of lateral signaling. *EMBO J.* **16**, 1647–1655 (1997).
7. Y. Yarden, A. Ullrich, Growth factor receptor tyrosine kinases. *Annu. Rev. Biochem.* **57**, 443–478 (1988).
8. G. Carpenter, S. Cohen, Epidermal growth factor. *J. Biol. Chem.* **265**, 7709–7712 (1990).
9. J. Baselga, S. M. Swain, Novel anticancer targets: Revisiting ERBB2 and discovering ERBB3. *Nat. Rev. Cancer* **9**, 463–475 (2009).
10. R. Roskoski Jr., The ErbB/HER family of protein-tyrosine kinases and cancer. *Pharmacol. Res.* **79**, 34–74 (2014).
11. J. Baselga, Why the epidermal growth factor receptor? The rationale for cancer therapy. *Oncologist* **7**, 2–8 (2002).
12. M. A. Lemmon, J. Schlessinger, Cell signaling by receptor tyrosine kinases. *Cell* **141**, 1117–1134 (2010).
13. P. Wu, T. E. Nielsen, M. H. Clausen, FDA-approved small-molecule kinase inhibitors. *Trends Pharmacol. Sci.* **36**, 422–439 (2015).
14. P. Wu, T. E. Nielsen, M. H. Clausen, Small-molecule kinase inhibitors: An analysis of FDA-approved drugs. *Drug Discov. Today* **21**, 5–10 (2016).
15. W. Cheng, Y. Hu, R. Sheng, Development of EGFR family small molecule inhibitors for anticancer intervention: An overview of approved drugs and clinical candidates. *Curr. Med. Chem.* **21**, 4374–4404 (2014).
16. N. E. Hynes, H. A. Lane, ERBB receptors and cancer: The complexity of targeted inhibitors. *Nat. Rev. Cancer* **5**, 341–354 (2005).
17. K. L. Blackwell, H. J. Burstein, A. M. Storniolo, H. S. Rugo, G. Sledge, G. Aktan, C. Ellis, A. Florance, S. Vukelja, J. Bischoff, J. Baselga, J. O'Shaughnessy, Overall survival benefit with lapatinib in combination with trastuzumab for patients with human Epidermal Growth Factor Receptor 2-positive metastatic breast cancer: Final results from the EGF104900 study. *J. Clin. Oncol.* **30**, 2585–2592 (2012).
18. C. E. Geyer, J. Forster, D. Lindquist, S. Chan, C. G. Romieu, T. Pienkowski, A. Jagiello-Gruszfeld, J. Crown, A. Chan, B. Kaufman, D. Skarlos, M. Campone, N. Davidson, M. Berger, C. Oliva, S. D. Rubin, S. Stein, D. Cameron, Lapatinib plus capecitabine for HER2-positive advanced breast cancer. *N. Engl. J. Med.* **355**, 2733–2743 (2006).
19. A. Di Leo, H. L. Gomez, Z. Aziz, Z. Zvirbule, J. Bines, M. C. Arbushites, S. F. Guerrera, M. Koehler, C. Oliva, S. H. Stein, L. S. Williams, J. Dering, R. S. Finn, M. F. Press, Phase III, double-blind, randomized study comparing lapatinib plus paclitaxel with placebo plus paclitaxel as first-line treatment for metastatic breast cancer. *J. Clin. Oncol.* **26**, 5544–5552 (2008).
20. S. T. Lee-Hoeflich, L. Crocker, E. Yao, T. Pham, X. Munroe, K. P. Hoeflich, M. X. Sliwkowski, H. M. Stern, A central role for HER3 in HER2-amplified breast cancer: Implications for targeted therapy. *Cancer Res.* **68**, 5878–5887 (2008).
21. S. M. Swain, D. Miles, S. B. Kim, Y. H. Im, S. A. Im, V. Semiglazov, E. Ciruelos, A. Schneeweiss, S. Loi, E. Monturus, E. Clark, A. Knott, E. Restuccia, M. C. Benyunes, J. Cortés, CLEOPARTRA study group, Pertuzumab, trastuzumab, and docetaxel for HER2-positive metastatic breast cancer (CLEOPATRA): End-of-study results from a double-blind, randomised, placebo-controlled, phase 3 study. *Lancet Oncol.* **21**, 519–530 (2020).
22. R. Nahta, M. C. Hung, F. J. Esteva, The HER-2-targeting antibodies trastuzumab and pertuzumab synergistically inhibit the survival of breast cancer cells. *Cancer Res.* **64**, 2343–2346 (2004).
23. J. Yu, T. Fang, C. Yun, X. Liu, X. Cai, Antibody-drug conjugates targeting the human epidermal growth factor receptor family in cancers. *Front. Mol. Biosci.* **9**, 847835 (2022).
24. M. Alimandi, A. Romano, M. C. Curia, R. Muraro, P. Fedi, S. A. Aaronson, P. P. Di Fiore, M. H. Kraus, Cooperative signaling of ErbB3 and ErbB2 in neoplastic transformation and human mammary carcinomas. *Oncogene* **10**, 1813–1821 (1995).
25. D. B. Vaught, J. C. Stanford, C. Young, D. J. Hicks, F. Wheeler, C. Rinehart, V. Sánchez, J. Koland, W. J. Muller, C. L. Arteaga, R. S. Cook, HER3 is required for HER2-induced preneoplastic changes to the breast epithelium and tumor formation. *Cancer Res.* **72**, 2672–2682 (2012).
26. T. Holbro, R. R. Beerli, F. Maurer, M. Koziczak, C. F. Barbas III, N. E. Hynes, The ErbB2/ErbB3 heterodimer functions as an oncogenic unit: ErbB2 requires ErbB3 to drive breast tumor cell proliferation. *Proc. Natl. Acad. Sci. U.S.A.* **100**, 8933–8938 (2003).
27. D. B. Agus, R. W. Akita, W. D. Fox, G. D. Lewis, B. Higgins, P. I. Pisacane, J. A. Lofgren, C. Tindell, D. P. Evans, K. Maiese, H. I. Scher, M. X. Sliwkowski, Targeting ligand-activated ErbB2 signaling inhibits breast and prostate tumor growth. *Cancer Cell* **2**, 127–137 (2002).
28. O. Metzger-Filho, E. P. Winer, I. Krop, Pertuzumab: Optimizing HER2 blockade. *Clin. Cancer Res.* **19**, 5552–5556 (2013).
29. R. Ghosh, A. Narasanna, S. E. Wang, S. Liu, A. Chakrabarty, J. M. Balko, A. M. González-Angulo, G. B. Mills, E. Penuel, J. Winslow, J. Sperinde, R. Dua, S. Pidaparthi, A. Mukherjee, K. Leitzel, W. J. Kostler, A. Lipton, M. Bates, C. L. Arteaga, Trastuzumab has preferential activity against breast cancers driven by HER2 homodimers. *Cancer Res.* **71**, 1871–1882 (2011).
30. D. Diwanji, R. Trenker, T. M. Thaker, F. Wang, D. A. Agard, K. A. Verba, N. Jura, Structures of the HER2-HER3-NRG1β complex reveal a dynamic dimer interface. *Nature* **600**, 339–343 (2021).
31. Y. Hao, X. Yu, Y. Bai, H. J. McBride, X. Huang, Cryo-EM structure of HER2-trastuzumab-pertuzumab complex. *PLOS ONE* **14**, e0216095 (2019).
32. T. P. Garrett, N. M. McKern, M. Lou, T. C. Elleman, T. E. Adams, G. O. Lovrecz, M. Kofler, R. N. Jorissen, E. C. Nice, A. W. Burgess, C. W. Ward, The crystal structure of a truncated ErbB2 ectodomain reveals an active conformation, poised to interact with other ErbB receptors. *Mol. Cell* **11**, 495–505 (2003).
33. K. Aertgeerts, R. Skene, J. Yano, B. C. Sang, H. Zou, G. Snell, A. Jennings, K. Iwamoto, N. Habuka, A. Hirokawa, T. Ishikawa, T. Tanaka, H. Miki, Y. Ohta, S. Sogabe, Structural analysis of the mechanism of inhibition and allosteric activation of the kinase domain of HER2 protein. *J. Biol. Chem.* **286**, 18756–18765 (2011).
34. E. V. Bocharov, K. S. Mineev, P. E. Volynsky, Y. S. Ermolyuk, E. N. Tkach, A. G. Sobol, V. V. Chupin, M. P. Kirpichnikov, R. G. Efremov, A. S. Arseniev, Spatial structure of the dimeric transmembrane domain of the growth factor receptor ErbB2 presumably corresponding to the receptor active state. *J. Biol. Chem.* **283**, 6950–6956 (2008).
35. C. Jost, J. Schilling, R. Tamaskovic, M. Schwill, A. Honegger, A. Plückthun, Structural basis for eliciting a cytotoxic effect in HER2-overexpressing cancer cells via binding to the extracellular domain of HER2. *Structure* **21**, 1979–1991 (2013).
36. P. E. Bragin, K. S. Mineev, O. V. Bocharova, P. E. Volynsky, E. V. Bocharov, A. S. Arseniev, HER2 transmembrane domain dimerization coupled with self-association of membrane-embedded cytoplasmic juxtamembrane regions. *J. Mol. Biol.* **428**, 52–61 (2016).
37. J. F. Franco-Gonzalez, V. L. Cruz, J. Ramos, J. Martinez-Salazar, Conformational flexibility of the ErbB2 ectodomain and trastuzumab antibody complex as revealed by molecular dynamics and principal component analysis. *J. Mol. Model.* **19**, 1227–1236 (2013).
38. T. T. Junttila, R. W. Akita, K. Parsons, C. Fields, G. D. Lewis Phillips, L. S. Friedman, D. Sampath, M. X. Sliwkowski, Ligand-independent HER2/HER3/PI3K complex is disrupted by trastuzumab and is effectively inhibited by the PI3K inhibitor GDC-0941. *Cancer Cell* **15**, 429–440 (2009).
39. R. Ruedas, R. Vuillemot, T. Tubiana, J. M. Winter, L. Pieri, A. A. Arteni, C. Samson, S. Jonic, M. Mathieu, S. Bressanelli, Structure and conformational variability of the HER2-trastuzumab-pertuzumab complex. *J. Struct. Biol.* **216**, 108095 (2024).
40. H. Maadi, M. H. Soheilifar, W. S. Choi, A. Moshtaghian, Z. Wang, Trastuzumab mechanism of action; 20 years of research to unravel a dilemma. *Cancers (Basel)* **13**, 3540 (2021).
41. L. Z. Mi, M. J. Grey, N. Nishida, T. Walz, C. Lu, T. A. Springer, Functional and structural stability of the epidermal growth factor receptor in detergent micelles and phospholipid nanodiscs. *Biochemistry* **47**, 10314–10323 (2008).
42. L. Z. Mi, C. Lu, Z. Li, N. Nishida, T. Walz, T. A. Springer, Simultaneous visualization of the extracellular and cytoplasmic domains of the epidermal growth factor receptor. *Nat. Struct. Mol. Biol.* **18**, 984–989 (2011).
43. C. O. S. Sorzano, A. Jiménez-Moreno, D. Maluenda, E. Ramirez-Aportela, M. Martínez, A. Cuervo, R. Melero, J. J. Conesa, R. Sanchez-Garcia, D. Strelak, J. Filipovic, E. Fernandez-Gimenez, F. de Isidro-Gomez, D. Herreros, P. Conesa, L. Del Cano, Y. Fonseca, J. J. de la Morena, J. R. Macias, P. Losana, R. Marabini, J. M. Carazo, Image processing in cryo-electron microscopy of single particles: The power of combining methods. *Methods Mol. Biol.* **2305**, 257–289 (2021).
44. Y. Huang, J. Ognjenovic, D. Karandur, K. Miller, A. Merk, S. Subramaniam, J. Kuriyan, A molecular mechanism for the generation of ligand-dependent differential outputs by the epidermal growth factor receptor. *eLife* **10**, e73218 (2021).
45. R. Trenker, D. Diwanji, T. Bingham, K. A. Verba, N. Jura, Structural dynamics of the active HER4 and HER2/HER4 complexes is finely tuned by different growth factors and glycosylation. *eLife* **12**, RP92873 (2024).
46. J. L. Vilas, H. D. Tagare, New measures of anisotropy of cryo-EM maps. *Nat. Methods* **20**, 1021–1024 (2023).
47. J. Li, E. Choi, H. Yu, X. C. Bai, Structural basis of the activation of type 1 insulin-like growth factor receptor. *Nat. Commun.* **10**, 4567 (2019).
48. E. Uchikawa, E. Choi, G. Shang, H. Yu, X. C. Bai, Activation mechanism of the insulin receptor revealed by cryo-EM structure of the fully liganded receptor-ligand complex. *eLife* **8**, e48630 (2019).
49. X. Zhang, D. Yu, J. Sun, Y. Wu, J. Gong, X. Li, L. Liu, S. Liu, J. Liu, Y. Wu, D. Li, Y. Ma, X. Han, Y. Zhu, Z. Wu, Y. Wang, Q. Ouyang, T. Wang, Visualization of ligand-bound ectodomain assembly in the full-length human IGF-1 receptor by cryo-EM single-particle analysis. *Structure* **28**, 555–561.e4 (2020).
50. R. Tamaskovic, M. Schwill, G. Nagy-Davidescu, C. Jost, D. C. Schaefer, W. P. Verdurmen, J. V. Schaefer, A. Honegger, A. Plückthun, Intermolecular biparatopic trapping of ErbB2 prevents compensatory activation of PI3K/AKT via RAS-p110 crosstalk. *Nat. Commun.* **7**, 11672 (2016).
51. F. Kast, M. Schwill, J. C. Stüber, S. Pfundstein, G. Nagy-Davidescu, J. M. M. Rodríguez, F. Seehusen, C. P. Richter, A. Honegger, K. P. Hartmann, T. G. Weber, F. Kroener, P. Ernst,

J. Piehler, A. Plückthun, Engineering an anti-HER2 biparatopic antibody with a multimodal mechanism of action. *Nat. Commun.* **12**, 3790 (2021).
52. J. C. Stüber, C. P. Richter, J. S. Bellón, M. Schwill, I. König, B. Schuler, J. Piehler, A. Plückthun, Apoptosis-inducing anti-HER2 agents operate through oligomerization-induced receptor immobilization. *Commun. Biol.* **4**, 762 (2021).
53. J. F. Vega, J. Ramos, V. L. Cruz, E. Vicente-Alique, E. Sanchez-Sanchez, A. Sanchez-Fernandez, Y. Wang, P. Hu, J. Cortes, J. Martinez-Salazar, Molecular and hydrodynamic properties of human epidermal growth factor receptor HER2 extracellular domain and its homodimer: Experiments and multi-scale simulations. *Biochim. Biophys. Acta Gen. Subj.* **1861**, 2406–2416 (2017).
54. G. Fuentes, M. Scaltriti, J. Baselga, C. S. Verma, Synergy between trastuzumab and pertuzumab for human epidermal growth factor 2 (Her2) from colocalization: An in silico based mechanism. *Breast Cancer Res.* **13**, R54 (2011).
55. E. Lobner, A. S. Humm, K. Goritzer, G. Mlynek, M. G. Puchinger, C. Hasenhindl, F. Rüker, M. W. Traxlmayr, K. Djinovic-Carugo, C. Obinger, Fcab-HER2 interaction: A menage a trois. Lessons from x-ray and solution studies. *Structure* **25**, 878–889.e5 (2017).
56. Z. Wang, L. Cheng, G. Guo, B. Cheng, S. Hu, H. Zhang, Z. Zhu, L. Niu, Structural insight into a matured humanized monoclonal antibody HuA21 against HER2-overexpressing cancer cells. *Acta Crystallogr. D Struct. Biol.* **75**, 554–563 (2019).
57. M. D'Huyvetter, J. De Vos, C. Xavier, M. Pruszynski, Y. G. J. Sterckx, S. Massa, G. Raes, V. Caveliers, M. R. Zalutsky, T. Lahoutte, N. Devoogdt, (131)I-labeled anti-HER2 camelid sdAb as a theranostic tool in cancer treatment. *Clin. Cancer Res.* **23**, 6616–6628 (2017).
58. J. Bostrom, S. F. Yu, D. Kan, B. A. Appleton, C. V. Lee, K. Billeci, W. Man, F. Peale, S. Ross, C. Wiesmann, G. Fuh, Variants of the antibody Herceptin that interact with HER2 and VEGF at the antigen binding site. *Science* **323**, 1610–1614 (2009).
59. C. Eigenbrot, M. Ultsch, A. Dubnovitsky, L. Abrahmsen, T. Hard, Structural basis for high-affinity HER2 receptor binding by an engineered protein. *Proc. Natl. Acad. Sci. U.S.A.* **107**, 15039–15044 (2010).
60. X. Bai, P. Sun, X. Wang, C. Long, S. Liao, S. Dang, S. Zhuang, Y. Du, X. Zhang, N. Li, K. He, Z. Zhang, Structure and dynamics of the EGFR/HER2 heterodimer. *Cell Discov.* **9**, 18 (2023).
61. D. Diwanji, R. Trenker, N. Jura, K. A. Verba, Efficient expression, purification, and visualization by cryo-EM of unliganded near full-length HER3. *Methods Enzymol.* **667**, 611–632 (2022).
62. A. P. Garner, C. U. Bialucha, E. R. Sprague, J. T. Garrett, Q. Sheng, S. Li, O. Sineshchekova, P. Saxena, C. R. Sutton, D. Chen, Y. Chen, H. Wang, J. Liang, R. Das, R. Mosher, J. Gu, A. Huang, N. Haubst, C. Zehetmeier, M. Haberl, W. Elis, C. Kunz, A. B. Heidt, K. Herlihy, J. Murtie, A. Schuller, C. L. Arteaga, W. R. Sellers, S. A. Ettenberg, An antibody that locks HER3 in the inactive conformation inhibits tumor growth driven by HER2 or neuregulin. *Cancer Res.* **73**, 6024–6035 (2013).
63. M. C. Franklin, K. D. Carey, F. F. Vajdos, D. J. Leahy, A. M. de Vos, M. X. Sliwkowski, Insights into ErbB signaling from the structure of the ErbB2-pertuzumab complex. *Cancer Cell* **5**, 317–328 (2004).
64. N. Gaborit, C. Larbouret, J. Vallaghe, F. Peyrusson, C. Bascoul-Mollevi, E. Crapez, D. Azria, T. Chardes, M. A. Poul, G. Mathis, H. Bazin, A. Pelegrin, Time-resolved fluorescence resonance energy transfer (TR-FRET) to analyze the disruption of EGFR/HER2 dimers: A new method to evaluate the efficiency of targeted therapy using monoclonal antibodies. *J. Biol. Chem.* **286**, 11337–11345 (2011).
65. S. Q. Zheng, E. Palovcak, J. P. Armache, K. A. Verba, Y. Cheng, D. A. Agard, MotionCor2: Anisotropic correction of beam-induced motion for improved cryo-electron microscopy. *Nat. Methods* **14**, 331–332 (2017).
66. J. M. de la Rosa-Trevin, A. Quintana, L. Del Cano, A. Zaldivar, I. Foche, J. Gutierrez, J. Gomez-Blanco, J. Burguet-Castell, J. Cuenca-Alba, V. Abrishami, J. Vargas, J. Oton, G. Sharov, J. L. Vilas, J. Navas, P. Conesa, M. Kazemi, R. Marabini, C. O. Sorzano, J. M. Carazo, Scipion: A software framework toward integration, reproducibility and validation in 3D electron microscopy. *J. Struct. Biol.* **195**, 93–99 (2016).
67. A. Rohou, N. Grigorieff, CTFFIND4: Fast and accurate defocus estimation from electron micrographs. *J. Struct. Biol.* **192**, 216–221 (2015).
68. T. Wagner, F. Merino, M. Stabrin, T. Moriya, C. Antoni, A. Apelbaum, P. Hagel, O. Sitsel, T. Raisch, D. Prumbaum, D. Quentin, D. Roderer, S. Tacke, B. Siebolds, E. Schubert, T. R. Shaikh, P. Lill, C. Gatsogiannis, S. Raunser, SPHIRE-crYOLO is a fast and accurate fully automated particle picker for cryo-EM. *Commun. Biol.* **2**, 218 (2019).
69. A. Punjani, J. L. Rubinstein, D. J. Fleet, M. A. Brubaker, cryoSPARC: Algorithms for rapid unsupervised cryo-EM structure determination. *Nat. Methods* **14**, 290–296 (2017).
70. A. Punjani, H. Zhang, D. J. Fleet, Non-uniform refinement: Adaptive regularization improves single-particle cryo-EM reconstruction. *Nat. Methods* **17**, 1214–1221 (2020).
71. K. Zhang, Gautomatch (2017); https://github.com/scipion-em/scipion-em-gautomatch.
72. R. Sanchez-Garcia, J. Gomez-Blanco, A. Cuervo, J. M. Carazo, C. O. S. Sorzano, J. Vargas, DeepEMhancer: A deep learning solution for cryo-EM volume post-processing. *Commun. Biol.* **4**, 874 (2021).
73. J. Zivanov, T. Nakane, B. O. Forsberg, D. Kimanius, W. J. Hagen, E. Lindahl, S. H. Scheres, New tools for automated high-resolution cryo-EM structure determination in RELION-3. *eLife* **7**, e42166 (2018).
74. J. L. Vilas, H. D. Tagare, J. Vargas, J. M. Carazo, C. O. S. Sorzano, Measuring local-directional resolution and local anisotropy in cryo-EM maps. *Nat. Commun.* **11**, 55 (2020).
75. E. C. Meng, T. D. Goddard, E. F. Pettersen, G. S. Couch, Z. J. Pearson, J. H. Morris, T. E. Ferrin, UCSF ChimeraX: Tools for structure building and analysis. *Protein Sci.* **32**, e4792 (2023).
76. J. K. Leman, B. D. Weitzner, S. M. Lewis, J. Adolf-Bryfogle, N. Alam, R. F. Alford, M. Aprahamian, D. Baker, K. A. Barlow, P. Barth, B. Basanta, B. J. Bender, K. Blacklock, J. Bonet, S. E. Boyken, P. Bradley, C. Bystroff, P. Conway, S. Cooper, B. E. Correia, B. Coventry, R. Das, R. M. De Jong, F. DiMaio, L. Dsilva, R. Dunbrack, A. S. Ford, B. Frenz, D. Y. Fu, C. Geniesse, L. Goldschmidt, R. Gowthaman, J. J. Gray, D. Gront, S. Guffy, S. Horowitz, P. S. Huang, T. Huber, T. M. Jacobs, J. R. Jeliazkov, D. K. Johnson, K. Kappel, J. Karanicolas, H. Khakzad, K. R. Khar, S. D. Khare, F. Khatib, A. Khramushin, I. C. King, R. Kleffner, B. Koepnick, T. Kortemme, G. Kuenze, B. Kuhlman, D. Kuroda, J. W. Labonte, J. K. Lai, G. Lapidoth, A. Leaver-Fay, S. Lindert, T. Linsky, N. London, J. H. Lubin, S. Lyskov, J. Maguire, L. Malmstrom, E. Marcos, O. Marcu, N. A. Marze, J. Meiler, R. Moretti, V. K. Mulligan, S. Nerli, C. Norn, S. O'Conchuir, N. Ollikainen, S. Ovchinnikov, M. S. Pacella, X. Pan, H. Park, R. E. Pavlovicz, M. Pethe, B. G. Pierce, K. B. Pilla, B. Raveh, P. D. Renfrew, S. S. R. Burman, A. Rubenstein, M. F. Sauer, A. Scheck, W. Schief, O. Schueler-Furman, Y. Sedan, A. M. Sevy, N. G. Sgourakis, L. Shi, J. B. Siegel, D. A. Silva, S. Smith, Y. Song, A. Stein, M. Szegedy, F. D. Teets, S. B. Thyme, R. Y. Wang, A. Watkins, L. Zimmerman, R. Bonneau, Macromolecular modeling and design in Rosetta: Recent methods and frameworks. *Nat. Methods* **17**, 665–680 (2020).
77. D. Liebschner, P. V. Afonine, M. L. Baker, G. Bunkoczi, V. B. Chen, T. I. Croll, B. Hintze, L. W. Hung, S. Jain, A. J. McCoy, N. W. Moriarty, R. D. Oeffner, B. K. Poon, M. G. Prisant, R. J. Read, J. S. Richardson, D. C. Richardson, M. D. Sammito, O. V. Sobolev, D. H. Stockwell, T. C. Terwilliger, A. G. Urzhumtsev, L. L. Videau, C. J. Williams, P. D. Adams, Macromolecular structure determination using x-rays, neutrons and electrons: Recent developments in Phenix. *Acta Crystallogr. D Struct. Biol.* **75**, 861–877 (2019).
78. P. Emsley, B. Lohkamp, W. G. Scott, K. Cowtan, Features and development of Coot. *Acta Crystallogr. D Biol. Crystallogr.* **66**, 486–501 (2010).
79. G. Pintilie, K. Zhang, Z. Su, S. Li, M. F. Schmid, W. Chiu, Measurement of atom resolvability in cryo-EM maps with Q-scores. *Nat. Methods* **17**, 328–334 (2020).
80. E. Fernandez-Gimenez, M. Martinez, R. Sanchez-Garcia, R. Marabini, E. Ramirez-Aportela, P. Conesa, J. M. Carazo, C. O. S. Sorzano, Cryo-EM density maps adjustment for subtraction, consensus and sharpening. *J. Struct. Biol.* **213**, 107780 (2021).
81. M. Schuster, M. Deluigi, M. Pantic, S. Vacca, C. Baumann, D. J. Scott, A. Plückthun, O. Zerbe, Optimizing the α_{1B}-adrenergic receptor for solution NMR studies. *Biochim. Biophys. Acta Biomembr.* **1862**, 183354 (2020).
82. A. Flayhan, H. D. T. Mertens, Y. Ural-Blimke, M. Martinez Molledo, D. I. Svergun, C. Low, Saposin lipid nanoparticles: A highly versatile and modular tool for membrane protein research. *Structure* **26**, 345–355.e5 (2018).
83. J. Jumper, R. Evans, A. Pritzel, T. Green, M. Figurnov, O. Ronneberger, K. Tunyasuvunakool, R. Bates, A. Zidek, A. Potapenko, A. Bridgland, C. Meyer, S. A. A. Kohl, A. J. Ballard, A. Cowie, B. Romera-Paredes, S. Nikolov, R. Jain, J. Adler, T. Back, S. Petersen, D. Reiman, E. Clancy, M. Zielinski, M. Steinegger, M. Pacholska, T. Berghammer, S. Bodenstein, D. Silver, O. Vinyals, A. W. Senior, K. Kavukcuoglu, P. Kohli, D. Hassabis, Highly accurate protein structure prediction with AlphaFold. *Nature* **596**, 583–589 (2021).
84. R. Evans, M. O'Neill, A. Pritzel, N. Antropova, A. Senior, T. Green, A. Žídek, R. Bates, S. Blackwell, J. Yim, O. Ronneberger, S. Bodenstein, M. Zielinski, A. Bridgland, A. Potapenko, A. Cowie, K. Tunyasuvunakool, R. Jain, E. Clancy, P. Kohli, J. Jumper, D. Hassabis, Protein complex prediction with AlphaFold-Multimer. bioRxiv 463034 [Preprint] (2022). https://doi.org/10.1101/2021.10.04.463034.
85. P. Littlefield, L. Liu, V. Mysore, Y. Shan, D. E. Shaw, N. Jura, Structural analysis of the EGFR/HER3 heterodimer reveals the molecular basis for activating HER3 mutations. *Sci. Signal.* **7**, ra114 (2014).
86. K. S. Mineev, N. F. Khabibullina, E. N. Lyukmanova, D. A. Dolgikh, M. P. Kirpichnikov, A. S. Arseniev, Spatial structure and dimer–monomer equilibrium of the ErbB3 transmembrane domain in DPC micelles. *Biochim. Biophys. Acta* **1808**, 2081–2088 (2011).
87. K. S. Mineev, E. V. Bocharov, Y. E. Pustovalova, O. V. Bocharova, V. V. Chupin, A. S. Arseniev, Spatial structure of the transmembrane domain heterodimer of ErbB1 and ErbB2 receptor tyrosine kinases. *J. Mol. Biol.* **400**, 231–243 (2010).
88. E. F. Pettersen, T. D. Goddard, C. C. Huang, E. C. Meng, G. S. Couch, T. I. Croll, J. H. Morris, T. E. Ferrin, UCSF ChimeraX: Structure visualization for researchers, educators, and developers. *Protein Sci.* **30**, 70–82 (2021).

Acknowledgments: We thank J. Stüber and Y. Waltenspühl for the support in the initial phases of the project. Imaging was performed with equipment maintained by the Center for Microscopy and Image Analysis (ZMB), University of Zürich, with particular thanks to S. Sorrentino. We further thank C. Löw for providing us with the saposin A vector and M. Schuster for providing us with the MSP1D1ΔH5 expression pellet. We also thank M. Iceta from CNB-CSIC

for the IT support and scripting and N. Larrieux, from Institut Pasteur Montevideo, for assistance in preparing the models for movie S1. **Funding:** This work was supported by the European Research Council grant HighResCells (ERC-2018-SyG, proposal: 810057) (to A.P., O.M., and J.M.C.); the Ministry of Science and Innovation/Spanish Agency for Science and Technology (MCIN/AEI) grant PID2022-136594NB-I00, with support from the European Regional Development Fund (ERDF)—"A way of making Europe." (to J.M.C.); the Ministry of Science and Innovation support for the Instruct Image Processing Center (I2PC) as part of the Spanish participation in Instruct-ERIC, the European Strategic Infrastructure Project (ESFRI) in the area of Structural Biology (BDNS no. 716450) (to J.M.C.); the Comunidad Autónoma de Madrid grant S2022/BMD-7232 (to J.M.C.); and the Scholarships from Institut Pasteur (Sejours Scientifiques program) and EU Horizon 2020 project EU-LAC ResInfra, which included access to the Instruct Image Processing Center with the financial support provided by Instruct-ERIC (APPID: 1750) (to A.B.). **Author contributions:** Cloning, expression, purification, amphipol reconstitution, MSP-based nanodisc reconstitution, preparation of complexes, cryo-EM sample preparation, and cryo-EM data acquisition were performed by S.V. Expression, purification of saposin A, and HER2 reconstitution into saposin A nanodiscs were performed by S.B.-G. under the supervision of S.V. S.V. and M.G. analyzed and interpreted cryo-EM data, with help from A.B., D.H., J.M.K., R.M., C.O.S.S., and J.M.C. Atomic model building, refinements, validation, and measurements with models were performed by A.B. and M.G. Project management was carried out by S.V., M.G., J.M.C., O.M., and A.P. The initial manuscript was prepared by S.V. and M.G. All authors contributed to the result interpretation and discussion, as well as to the final editing and approval of the manuscript. **Competing interests:** The authors declare that they have no competing interests. **Data and materials availability:** The cryo-EM maps of the HER2 ECD from the Apo dataset and the extended and compact maps from the TZB dataset have been deposited in Electron Microscopy Data Bank under the accession codes EMD-52999, EMD-52998, and EMD-52997, respectively. The atomic coordinates derived from these maps have been deposited in the PDB under accession codes 9QBH, 9QBG, and 9QBF, respectively. All data needed to evaluate the conclusions in the paper are present in the paper and/or the Supplementary Materials.

Submitted 2 December 2024
Accepted 23 June 2025
Published 25 July 2025
10.1126/sciadv.adu9945